ACS APPLIED MATERIALS & INTERFACES

Research Article

www.acsami.org

Phase Tuning of Nanostructured Gallium Oxide via Hybridization with Reduced Graphene Oxide for Superior Anode Performance in Li-Ion Battery: An Experimental and Theoretical Study

Sharad B. Patil,[†] In Young Kim,[†] Jayavant L. Gunjakar,[†] Seung Mi Oh,[†] Taedaehyeong Eom,[‡] Hyungjun Kim,[‡] and Seong-Ju Hwang*[,†]

[†]Department of Chemistry and Nanoscience, College of Natural Sciences, Ewha Womans University, Seoul 120-750, Korea

[‡]Graduate School of Energy, Environment, Water, and Sustainability (EEWS), Korea Advanced Institute of Science and Technology (KAIST), Daejon 305-701, Korea

Supporting Information

ABSTRACT: The crystal phase of nanostructured metal oxide can be effectively controlled by the hybridization of gallium oxide with reduced graphene oxide (rGO) at variable concentrations. The change of the ratio of Ga_2O_3/rGO is quite effective in tailoring the crystal structure and morphology of nanostructured gallium oxide hybridized with rGO. This is the first example of the phase control of metal oxide through a change of the content of rGO hybridized. The calculations based on density functional theory (DFT) clearly demonstrate that the different surface formation energy and Ga local symmetry of Ga_2O_3 phases are responsible for the phase transition induced by the change of rGO content. The resulting Ga_2O_3−rGO nanocomposites show promising electrode performance for lithium ion batteries. The intermediate Li−Ga alloy phases formed during the electrochemical cycling are identified with the DFT calculations. Among the present Ga_2O_3−rGO nanocomposites, the material with mixed α-Ga_2O_3/β-Ga_2O_3/γ-Ga_2O_3 phase can deliver the largest discharge capacity with the best cyclability and rate characteristics, highlighting the importance of the control of Ga_2O_3/rGO ratio in optimizing the electrode activity of the composite materials. The present study underscores the usefulness of the phase-control of nanostructured metal oxides achieved by the change of rGO content in exploring novel functional nanocomposite materials.

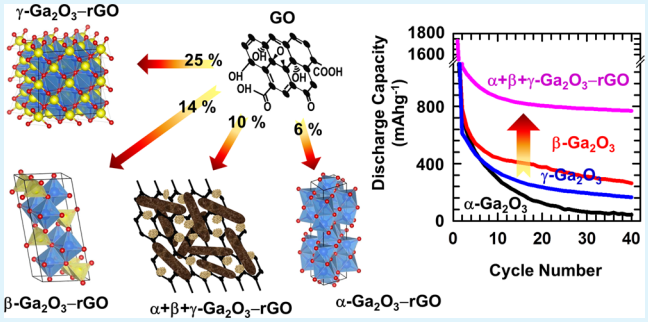

KEYWORDS: *phase control, gallium oxide, reduced graphene oxide, nanocomposite, electrode materials*

1. INTRODUCTION

As an emerging member of nanostructured carbon species, reduced graphene oxide (rGO) attracts a great deal of research activity due to its unique physicochemical properties such as high electrical and thermal conductivity and high mechanical strength, as well as its valuable functionalities for diverse energy- and biorelated applications.[1,2] The expanded 2D surface of rGO nanosheet renders this material an effective matrix to immobilize diverse chemical species such as inorganic/organic nanostructures, polymers, and biomolecules.[2−6] The hybridization with rGO is quite effective in improving the functionalities of metal oxides such as electrochemical activity, catalytic activity, and mechanical strength.[7−14] Additionally, the hybridization of metal oxide on the 2D surface of rGO nanosheet has significant influence on its growth habit and crystal size, leading to the enhanced stability of the layered crystal structure and sheet-like morphology of metal oxides.[15] As a consequence, the rGO nanosheet can serve as a catalyst for accelerating the synthesis of 2D nanostructured metal oxide.[15] Such a prominent effect of hybridization with rGO would originate from a significant modification of the surface energy of hybridized metal oxides. Taking into account that nanostructured metal oxides possess a large proportion of surface species, the relative phase stability of these materials can be remarkably altered by the hybridization with rGO. This effect would make possible a tunable phase transition of hybridized metal oxides via the change of rGO content. Because many functionalities and properties of metal oxides strongly depend on their crystal structure, it is of prime importance to freely tailor the crystal phase of nanostructured metal oxides for their efficient applications. Although the hybridization with rGO is widely used for improving the electrical conductivity and porosity of metal oxides and for stabilizing the sheet-like morphology of metal oxides,[15] we are aware of no other report on the phase-tuning of hybridized metal oxides via the change of rGO content. Like other post-transition metal oxides, gallium oxide is expected to have a high reactivity for lithium ions, suggesting its applicability as electrode for lithium ion batteries.

Received: June 11, 2015
Accepted: August 10, 2015
Published: August 10, 2015

DOI: 10.1021/acsami.5b05154
ACS Appl. Mater. Interfaces 2015, 7, 18679−18688

Because there are several polymorphs of gallium oxide, the hybridization with rGO is supposed to significantly alter the relative stability of these Ga_2O_3 phases.[16] Thus, gallium oxide can be a good candidate for probing the effect of rGO content on the phase stability and electrochemical properties of metal oxide hybridized with rGO. The control of Ga_2O_3/rGO ratio can provide opportunity not only to tailor the crystal structure and crystal morphology of gallium oxide but also to optimize the electrode functionality of the gallium oxide−rGO nanocomposites. To the best of our knowledge, the nanocomposite electrode material consisting of nanostructured Ga_2O_3 and rGO has not been studied yet.

In the present study, a phase- and morphology-tunable synthesis of mesoporous Ga_2O_3−rGO nanocomposites can be achieved by the crystal growth of GaOOH in the presence of graphene oxide (GO) precursor and the following phase transition at elevated temperature. Because the GO precursor is reduced to rGO during the synthesis, the resulting nanocomposites can be described as Ga_2O_3−rGO nanocomposites. To probe the effect of rGO content on the structural and electrochemical properties of the nanocomposites, the Ga_2O_3−rGO nanocomposites are synthesized with several Ga/GO mass ratios of 2, 4, 6, and 8. Along with the experimental studies, DFT calculations are applied for elucidating the effect of crystal phase on the surface energy of Ga_2O_3 materials and for probing intermediate phases formed during the electrochemical cycling of Ga_2O_3.

2. EXPERIMENTAL SECTION

2.1. Synthesis of Nanocomposites. The aqueous colloidal suspension of GO nanosheets was prepared by modified Hummer's method.[17] The precursor GaOOH−rGO nanocomposites with several Ga/GO ratios were prepared by the hydrolysis of $Ga(NO_3)_3{\cdot}xH_2O$ (Sigma-Aldrich 99.9%) in the presence of colloidal GO suspension containing urea. In a typical synthesis, $Ga(NO_3)_3{\cdot}xH_2O$ was dissolved in the aqueous colloidal suspension of 0.05 wt % exfoliated GO nanosheets. After 15 min of stirring, urea (12 times larger moles than gallium nitrate) was slowly added and kept stirring for another 15 min. The bath temperature was slowly increased to 95 °C and maintained for 1 h under reflux condition. The product was centrifuged and washed with distilled water, which was followed by repeated washing with 2-propanol to completely remove residual urea. The obtained product was dried overnight at 50 °C. After the completion of the reaction, the remaining supernatant solution became transparent. The addition of ammonium hydroxide into the residual solution caused no precipitation of gallium oxide, confirming the complete incorporation of gallium ions into the nanocomposite lattice. The transformation of GaOOH component in the obtained nanocomposites into Ga_2O_3 was achieved by heat-treatment at 600 °C for 6 h in Ar atmosphere. As a reference, unhybridized α-Ga_2O_3 nanorod was prepared with the same synthesis process except the absence of GO nanosheets. The reference β-Ga_2O_3 was prepared by heating GaOOH at 600 °C for 12 h. To prepare the reference γ-Ga_2O_3, diluted aqueous ammonia (50% v/v in ethanol) was dropwise added to the ethanolic solution of $Ga(NO_3)_3{\cdot}xH_2O$ with constant stirring at room temperature until no further precipitation. The obtained precipitate was washed thoroughly with ethanol, dried under vacuum, and finally heated at 300 °C for 30 min.[18]

2.2. Characterization. The powder X-ray diffraction (XRD) analysis was done using a Rigaku diffractometer with Ni-filtered Cu Kα radiations. The thermogravimetric analysis (TGA) data were recorded on TA Instruments SDT Q600 at a rate of 10 °C min^{-1} in ambient atmosphere. The transmission electron microscopic (TEM) and field emission-scanning electron microscopy (FE-SEM) micrographs were captured on Jeol JEM-2100F and Jeol JSM-6700F electron microscopes, respectively. The N_2 adsorption−desorption isotherms were recorded at liquid nitrogen temperature using Micromeritics ASAP 2020. The samples were degassed at 150 °C for 5 h under vacuum before the adsorption measurement. X-ray photoelectron spectroscopic (XPS) data were recorded with a PHI 5100 PerkinElmer spectrometer. Micro-Raman spectra were collected with Horiba Jobin-Yvon LabRam Aramis spectrometer using diode laser with a wavelength of 785 nm as the excitation source. X-ray absorption spectra (XAS) at Ga K-edge were collected with extended X-ray absorption fine structure (EXAFS) facility installed at beamline 10C at the Pohang Accelerator Laboratory (PAL, Pohang, Korea). The voltage and current of synchrotron electron beam were 2.5 GeV and 180 mA, respectively. The present XAS data were collected in a transmission mode from the thin layer of powder samples deposited on transparent adhesive tapes using gas-ionization detectors. All the present XAS data were carefully calibrated by measuring the reference spectrum of Ga_2O_3 simultaneously. The data processing was done using Ifeffit (version 0.9.13) program.

2.3. Electrochemical Measurements. The electrochemical measurements were carried out with cells consisting of Li/1 M $LiPF_6$ in ethylene carbonate/diethyl carbonate (EC/DEC) (50:50 v/v)/composite electrode. The working electrodes were prepared by pasting slurry on copper foil, which was followed by vacuum drying at 120 °C for 12 h. The slurry was composed of active electrode material, Super P, and polyvinylidenefluoride (PVDF) in the weight ratio of 75:15:10 in *N*-methyl-2-pyrrolidene (NMP). The working electrode, Li counter electrode, and separator were assembled into 2016 coin-type cells in an argon-filled glovebox. The charge−discharge cycle data were recorded in a voltage window of 0.01−2.5 V at 25 °C using a MACCOR series 4000 cycler. Cyclic voltammogram (CV) data were recorded on an electrochemical workstation IVIUMSTAT in the potential range of 0.01−2.5 V with a scan rate of 0.2 mVs^{-1}. Electrochemical impedance spectroscopy (EIS) data were measured using IVIUM impedance analyzer in the frequency range of 100 kHz to 10 mHz at open circuit potential. The fitting analysis for the EIS spectra was performed using the ZView2 program.

2.4. DFT Calculations. All the DFT calculations were performed using Vienna Ab initio Simulation Package (VASP) using the choice of exchange-correlation functional of Perdue−Burke−Ernzerhof (PBE).[19,20] The DFT optimized structures of gallium oxide phases with computational details are presented in the Supporting Information (Figure S1 and Tables S1−S3). To construct a stoichiometric model of γ-Ga_2O_3 phase from inorganic crystal structure database (ICSD) structure consisting of partial occupancies of Ga, we used 1 × 1 × 3 supercell of primitive cell structure. Then, we randomly selected 4 "Ga" positions from 36 "Ga" sites having partial occupancy of 0.122 (4/36 = 0.111), 7 "Ga" positions from 12 "Ga" sites having partial occupancy of 0.569 (7/12 = 0.583), and 5 "Ga" position from 6 "Ga" sites having partial occupancy of 0.797 (5/6 = 0.833), yielding γ-Ga_2O_3 model structure composed of 16 "Ga" atoms and 24 "O" atoms in the simulation cell.

3. RESULTS AND DISCUSSION

3.1. TGA and Powder XRD Analyses. To determine the amount of rGO component, the thermal behaviors of the Ga_2O_3−rGO nanocomposites are studied with TGA. All the Ga_2O_3−rGO nanocomposites display a small mass loss of <2% below 150 °C, which is attributed to the removal of surface functional groups of the rGO (Figure S2). This mass loss becomes greater with the increase of rGO content. In the higher temperature region of 470−600 °C, all the present nanocomposites show significant mass loss corresponding to the combustion of graphitic carbon species. Beyond 600 °C, there is no significant mass loss, confirming the complete combustion of rGO species below this temperature. On the basis of the present TGA results, the content of rGO is estimated to be 25, 14, 10, and 6% for the nanocomposites with the Ga/GO mass ratios of 2, 4, 6, and 8, respectively.

DOI: 10.1021/acsami.5b05154
ACS Appl. Mater. Interfaces 2015, 7, 18679−18688

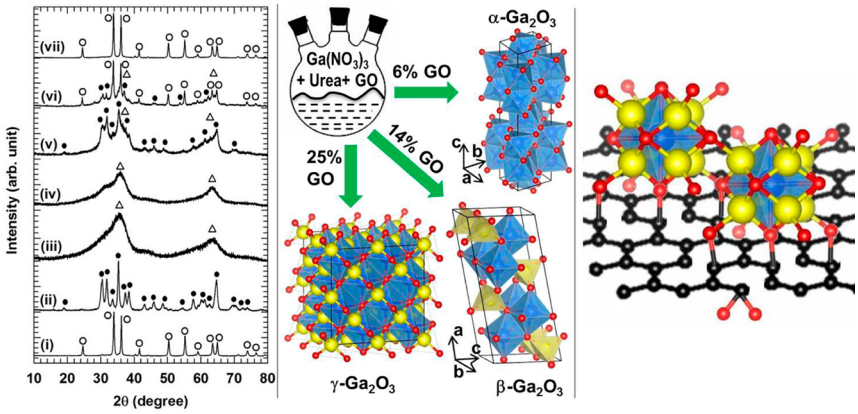

Figure 1. (Left) Powder XRD patterns of references (i) α-Ga_2O_3, (ii) β-Ga_2O_3, and (iii) γ-Ga_2O_3 and of the Ga_2O_3–rGO nanocomposites with rGO contents of (iv) 25, (v) 14, (vi) 10, and (vii) 6% with Bragg reflections of (○) α-Ga_2O_3, (●) β-Ga_2O_3, and (△) γ-Ga_2O_3 phases. Schematic models for (middle) phase transition of Ga_2O_3 induced by hybridization with rGO and (right) the stabilization of Ga_2O_3 phase by oxygenated group of rGO. Three-dimensional crystal structures represented by (blue) octahedral Ga, (yellow) tetrahedral Ga, and (red) O atoms with (line) a unit cell.

The crystal structures of the as-prepared GaOOH–rGO nanocomposites and their calcined derivatives are studied with powder XRD analysis. The as-prepared nanocomposites, except the materials with lowest Ga/rGO ratio, show distinct Bragg reflections of α-GaOOH phase, indicating the formation of gallium oxyhydroxide (Figure S3).[21] Although carbon usually acts as a reductive species for metal oxide,[22,23] the use of GO precursor in the present study does not cause the reduction of Ga^{3+} ions during the synthesis of the nanocomposites. This is attributable to the presence of oxygenated groups in the GO precursor. As the ratio of Ga/rGO decreases, the Bragg reflections of gallium oxyhydroxide become less distinct, showing the decrease of the crystal size and crystallinity of α-GaOOH upon the increase of rGO content. This observation is attributable to the provision of more seeding sites by the incorporation of larger amount of rGO nanosheets.

To induce a phase transition from gallium oxyhydroxide to gallium oxide, the as-prepared GaOOH–rGO nanocomposites are calcined at 600 °C. As plotted in the left panel of Figure 1, after the heat-treatment, the GaOOH component in the as-prepared nanocomposites changes to α-/β-/γ-Ga_2O_3 phases depending on the content of rGO nanosheet, indicating the profound effect of rGO nanosheet on the crystal growth of hybridized Ga_2O_3. The obtained Ga_2O_3–rGO nanocomposite with 25% rGO shows two broad but distinct Bragg reflections of γ-Ga_2O_3, whereas well-developed XRD peaks of β-Ga_2O_3 phase are clearly discernible for the nanocomposite with 14% rGO.[16,21] A further decrease of the rGO content leads to the formation of pure α-Ga_2O_3 (JCPDS-85-0988) in the nanocomposite with 6% rGO and main α-Ga_2O_3 phase with small amount of β- and γ-Ga_2O_3 phases in the nanocomposite with 10% rGO. As illustrated in the middle panel of Figure 1, this result clearly demonstrates the tunability of the crystal structure of hybridized Ga_2O_3 through the change of the rGO content. To the best of our knowledge, this is the first example of the phase control of metal oxide via the change of hybridized rGO content. Because α-Ga_2O_3 forms at low temperature of <700 °C and β-Ga_2O_3 is stable at higher temperature, the presence of α-Ga_2O_3 in the Ga_2O_3–rGO nanocomposite with 6% rGO prepared at 600 °C seems to be consistent with the reported phase transition behavior.[21] The phase transformation from α-Ga_2O_3 to β-/γ-Ga_2O_3 upon the increase of rGO content clearly demonstrates the stabilization of high-temperature phases via the hybridization with rGO nanosheets. In contrast to the Bragg reflections of Ga_2O_3 phases, no rGO-related XRD peaks are observable for all the nanocomposites, indicating the good dispersion of rGO nanosheets without phase segregation.

In addition to the crystal structure, the content of rGO nanosheet has significant influence on the crystal size of the Ga_2O_3. According to the crystal size calculation based on Scherrer formula, the average crystal size of the hybridized Ga_2O_3 is estimated to be 2, 11, 19, and 26 nm for the nanocomposites with the rGO contents of 25, 14, 10, and 6%, respectively. This result provides strong evidence for the control of particle size by changing the ratio of Ga/rGO, which can be ascribed to the provision of more seeding sites by the increase of rGO content.

The DFT calculations are utilized to understand the effect of rGO content on the phase stability of Ga_2O_3. According to the DFT analysis, β-Ga_2O_3 is only 0.15 eV f.u.$^{-1}$ more stable than α-Ga_2O_3 and γ-Ga_2O_3 is more unstable than the other two phases (0.42 eV f.u.$^{-1}$ more unstable than β-phase).[24] In contrast to the similar stability of the α- and β-phases, the surface formation energy of β-Ga_2O_3 is much lower than that of α-Ga_2O_3 (24.61 meV Å^{-2} for (100) surface of β-Ga_2O_3 vs 76.63 meV Å^{-2} for (110) surface of α-Ga_2O_3). This tendency can be attributed to the higher concentration of undercoordinated Ga on the surface of α-phase; for α-Ga_2O_3 consisting of only octahedral Ga in the bulk, all surface Ga atoms are undercoordinated. Conversely, for β-Ga_2O_3 consisting of octahedral Ga and tetrahedral Ga in the bulk, only octahedral Ga atoms are undercoordinated while the tetrahedral Ga atoms remain intact at the surface (Figure S4). Taking into account the decrease of crystal size upon the increase of rGO content, the β-Ga_2O_3 becomes more stable than the α-Ga_2O_3 one for the Ga_2O_3–rGO nanocomposites with lower Ga_2O_3/rGO ratios. This may explain the experimentally observed phase tunability achieved by varying rGO contents, because the surface stability becomes critical in determining the phase stability of nanoparticles due to the substantially increased surface-to-volume ratio caused by the decrease of particle size. Due to the presence of considerable Ga partial occupancy in γ-Ga_2O_3, it is difficult to exactly calculate the surface formation energy of this phase. However, like the β-Ga_2O_3, the hybridization with a large amount of rGO nanosheet can induce the stabilization of the most unstable γ-Ga_2O_3 phase in

DOI: 10.1021/acsami.5b05154
ACS Appl. Mater. Interfaces 2015, 7, 18679–18688

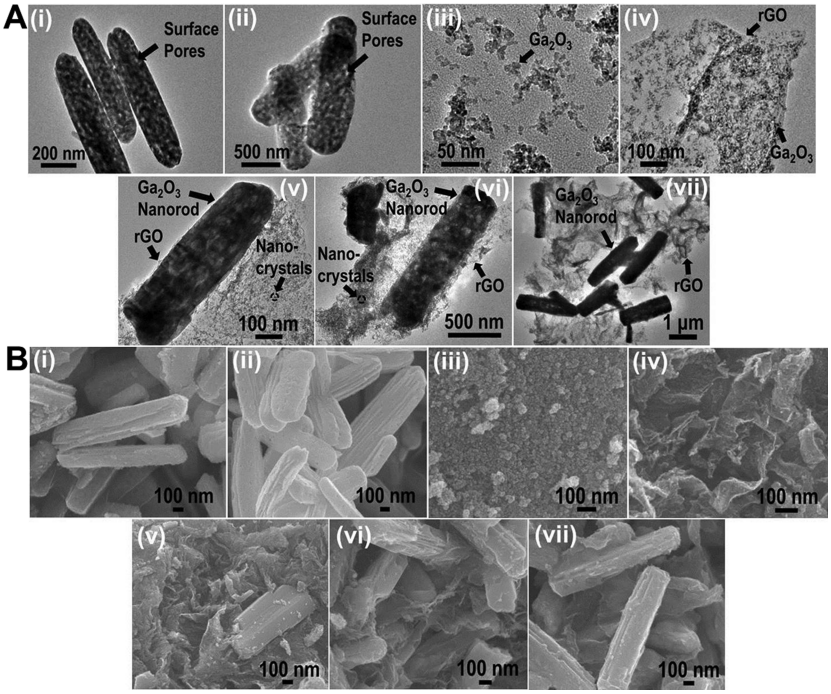

Figure 2. (A) TEM micrographs and (B) FE-SEM micrographs of references (i) α-Ga_2O_3, (ii) β-Ga_2O_3, (iii) γ-Ga_2O_3, and the Ga_2O_3–rGO nanocomposites with rGO contents of (iv) 25, (v) 14, (vi) 10, and (vii) 6%.

the nanocomposite with 25% rGO through the decrease of particle size, since the γ-Ga_2O_3 has many partially occupied Ga sites implying low surface formation energy. Also the coordination of Ga^{3+} ions by oxygenated surface functional groups of rGO helps to stabilize the γ-Ga_2O_3 and β-Ga_2O_3 phases having many partially occupied Ga sites, as depicted in the right panel of Figure 1. This stabilization effect is mainly responsible for the formation of unstable γ-Ga_2O_3 and β-Ga_2O_3 phases upon the hybridization with large amount of rGO nanosheet.

Although all the present data were obtained from the Ga_2O_3–rGO nanocomposites prepared with the GO precursor, we also adopted the rGO precursor to probe the effect of graphene precursor on the phase transformation behaviors of the Ga_2O_3–rGO nanocomposites. According to the powder XRD analysis (Figure S5), the Ga_2O_3–rGO nanocomposites prepared with the rGO precursor experience distinct dependence of the crystal structure of Ga_2O_3 component on the ratio of Ga_2O_3/rGO precursors, which are different from the phase transition behavior of the homologues prepared with the GO precursor; the Ga_2O_3–rGO nanocomposite prepared with the 25% rGO precursor shows the presence of mixed α- and β-Ga_2O_3 phases, which is sharply contrasted with the formation of γ-Ga_2O_3 phase for the nanocomposite prepared with the 25% GO precursor. This reflects that the use of GO precursor helps to stabilize γ-Ga_2O_3 through the coordination by surface-oxygenated groups. On the contrary, only the β-Ga_2O_3 phase is formed for the other nanocomposites with the rGO precursors (14, 10, and 6%). Additionally, beyond the rGO content of 14%, a distinct rGO-related peak appears in the XRD pattern, indicating the phase segregation of rGO phase. This is due to a stronger π–π interaction of the rGO nanosheets, as compared with the GO nanosheets. The present findings clearly demonstrate an inferior role of the rGO nanosheet as a precursor for the phase-tunable synthesis of the Ga_2O_3–rGO nanocomposites with homogeneous composite structure.

3.2. TEM and FE-SEM Analyses. Figure 2A represents the TEM images of the present Ga_2O_3–rGO nanocomposites prepared with the GO precursor and the Ga_2O_3 references with α-, β-, and γ-phases. The unhybridized α-Ga_2O_3 reference displays 1D nanorod-type morphology with needle-like ends, which originates from the fast growth of gallium oxide along the [001] direction.[21] The aspect ratio of α-Ga_2O_3 nanorod is determined to be ~6 with the diameter of ~140–180 nm and the length of ~0.75–1.25 μm. A close inspection reveals that each nanorod is polycrystalline and composed of primary crystallites of 25 nm in size, as estimated from powder XRD analysis. Similarly, the reference β-Ga_2O_3 material displays 1D nanorod morphology with a diameter of ~370–550 nm and a length of ~1.40–2.20 μm, which correspond to an aspect ratio of 3.5–5. Both the α-Ga_2O_3 and β-Ga_2O_3 references display large numbers of nanosized surface pores with a diameter of ~15 and ~20 nm, respectively, which are formed by the removal of hydroxyl groups in the precursor gallium oxyhydroxide.[21] In contrast to the present α-Ga_2O_3 and β-Ga_2O_3 materials, the reference γ-Ga_2O_3 is composed of very small crystallites with a size of ~5 nm.

The nanocomposite with 25% rGO shows the stabilization of Ga_2O_3 nanocrystals (the diameter of <5 nm) on the surface of rGO nanosheet, reflecting the formation of γ-Ga_2O_3 material. In the nanocomposites with rGO contents of 14 and 10%, the 1D nanorods with the diameter of ~200 nm and the length of ~750 nm are anchored on the rGO nanosheet together with smaller amount of nanocrystals of ~10 nm, suggesting the presence of α-/β- and γ-Ga_2O_3 phases. The nanocomposite with 6% rGO shows the anchoring of 1D nanorods on the surface of rGO nanosheets, indicating the formation of α-Ga_2O_3 phase. The decrease of rGO content in the nanocomposites gives rise to the distinct enlargement of Ga_2O_3 nanocrystals/nanorods. The sizes of primary gallium oxide crystals in the present nanocomposites determined by the TEM

DOI: 10.1021/acsami.5b05154
ACS Appl. Mater. Interfaces 2015, 7, 18679–18688

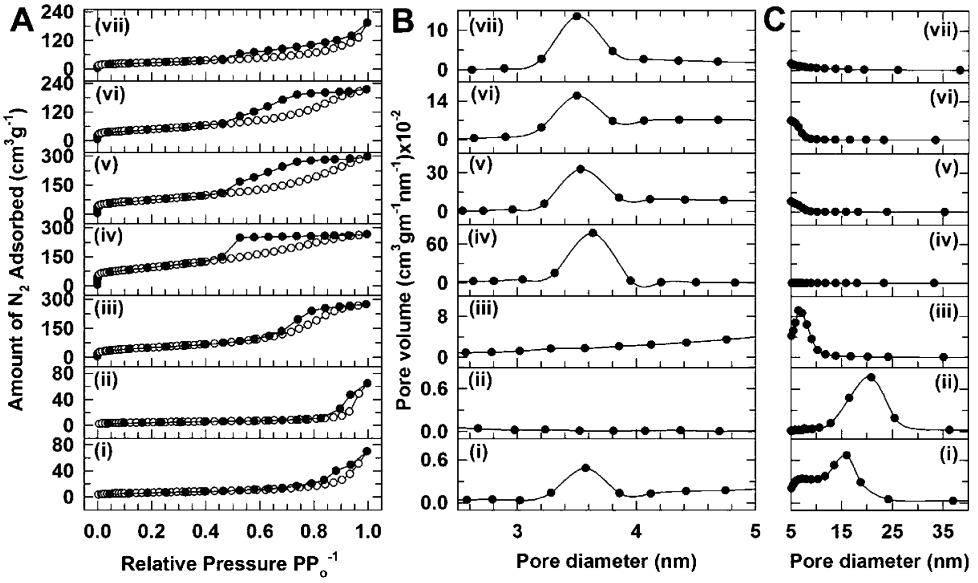

Figure 3. (A) N_2 adsorption−desorption isotherms and (B and C) pore size distribution curves of references (i) α-Ga_2O_3, (ii) β-Ga_2O_3, and (iii) γ-Ga_2O_3 and the Ga_2O_3−rGO nanocomposites with rGO contents of (iv) 25, (v) 14, (vi) 10, and (vii) 6%.

analysis are in good agreement with those calculated with Scherrer formula.

The FE-SEM images of the Ga_2O_3−rGO nanocomposites are illustrated in Figure 2B, as compared with the unhybridized Ga_2O_3 references. All the present nanocomposites display mesoporous stacking structure composed of sheet-like crystallites, which becomes less prominent with the increase of Ga/rGO ratio. This strongly suggests the significant contribution of rGO nanosheets in forming the mesoporous stacking morphology of the nanocomposites. The present FE-SEM data exhibit gradual variations of the crystal shape and size of Ga_2O_3 in the nanocomposites, which is in good agreement with the TEM results.

Summarizing the present XRD, TEM, and FE-SEM results, the increase of Ga/rGO ratio leads not only to the phase transformation of γ-Ga_2O_3 → β-Ga_2O_3 → α-Ga_2O_3 but also to the increase of the crystal size of Ga_2O_3. The provision of a larger amount of Ga precursor is responsible for the observed enlargement of Ga_2O_3 crystals with increasing the Ga/rGO ratio. As predicted by the DFT calculation, the increase of crystal size with the decrease of surface area enhances the relative phase stability of the α-Ga_2O_3 phase having octahedral GaO_6 symmetry compared with the β-Ga_2O_3/γ-Ga_2O_3 phase having lower average coordination numbers. Such a variation of relative phase stability is responsible for the phase transformation caused by the change of Ga/rGO ratio.

3.3. N_2 Adsorption−Desorption Isotherm Measurement. The effects of the hybridization with the rGO nanosheet on the surface area and porosity of Ga_2O_3 are investigated by N_2 adsorption−desorption isotherm measurements. The resulting isotherms are presented in Figure 3A. In comparison with the references α-Ga_2O_3 and β-Ga_2O_3, all of the Ga_2O_3−rGO nanocomposites demonstrate much more efficient adsorption of N_2 molecules, strongly suggesting the increase of surface area upon hybridization with rGO. In the pressure region of $pp_o^{-1} > 0.4$, all the present nanocomposites exhibit more prominent hysteresis than do the unhybridized Ga_2O_3 references, reflecting the formation of mesopores upon the hybridization with rGO. The observed isotherms of the Ga_2O_3−rGO nanocomposites with the rGO contents of 25, 14, and 10% can be classified as Brunauer−Deming−Deming−Teller (BDDT)-type I and IV shapes of isotherms and an H2-type hysteresis loop in the IUPAC classification, demonstrating the presence of open slit-shaped capillaries with very wide bodies and narrow short necks.[25−27] This type of isotherm is frequently observed for the mesoporous stacking structure of sheet-like 2D crystallites.[25] The nanocomposite with 6% rGO exhibits BDDT-type I and IV shape of isotherms with an H3-type hysteresis loop in the IUPAC classification. The references α-Ga_2O_3 and β-Ga_2O_3 commonly display BDDT-type IV shape of isotherms and H3-type weak hysteresis loop in the IUPAC classification, which is typically observed for the aggregates of plate-like particles with slit-shaped mesopores.[25,26] Conversely, the reference γ-Ga_2O_3 displays BDDT-type I and V shapes of isotherms with an H1-type hysteresis loop, which are characteristics of the agglomerates of uniform spherical particles.[25,26] According to the fitting analysis based on the Brunauer−Emmett−Teller (BET) equation, the hybridization with rGO nanosheets leads to the remarkable expansion of surface area to ∼340, ∼ 264, ∼ 172, and ∼97 m^2g^{-1} for the nanocomposites with the rGO contents of 25, 14, 10, and 6%, respectively. This result confirms that the increase of rGO content causes the increase of surface area. In comparison with the present Ga_2O_3−rGO nanocomposites, both the references α-Ga_2O_3 and β-Ga_2O_3 possess much smaller surface area of ∼23 and ∼16 m^2g^{-1}, respectively, whereas a comparable surface area of ∼184 m^2g^{-1} occurs for the γ-Ga_2O_3 reference.

According to the calculation of pore size distribution on the basis of the Barrett−Joyner−Halenda (BJH) method, all of the Ga_2O_3−rGO nanocomposites possess relatively narrow distribution of mesopores with an average diameter of ∼3−4 nm (Figure 3B), confirming the formation of regular mesoporous materials. The formation of mesopores is attributable to the house-of-cards-type stacking of nanocomposite of 2D crystallites. In contrast to the present nanocomposites, the reference α-Ga_2O_3 shows an additional peak around 15 nm, which corresponds to the surface pores of Ga_2O_3 nanorods (Figure 3C). The reference β-Ga_2O_3 exhibits a peak centered at 20 nm,

DOI: 10.1021/acsami.5b05154
ACS Appl. Mater. Interfaces 2015, 7, 18679−18688

indicating the enlargement of pore size after the extended heat-treatment, as found from the TEM images. Conversely, a narrow distribution of pores with small diameter of ~6 nm is observed for the reference γ-Ga_2O_3.

3.4. XPS, Micro-Raman and FT-IR Analyses. The effect of composite formation on the chemical bonding nature of the Ga_2O_3 and rGO is investigated with the XPS, micro-Raman and Fourier transformed-infrared (FT-IR) spectroscopies. As can be seen from Figure 4A, all of the present Ga_2O_3–rGO

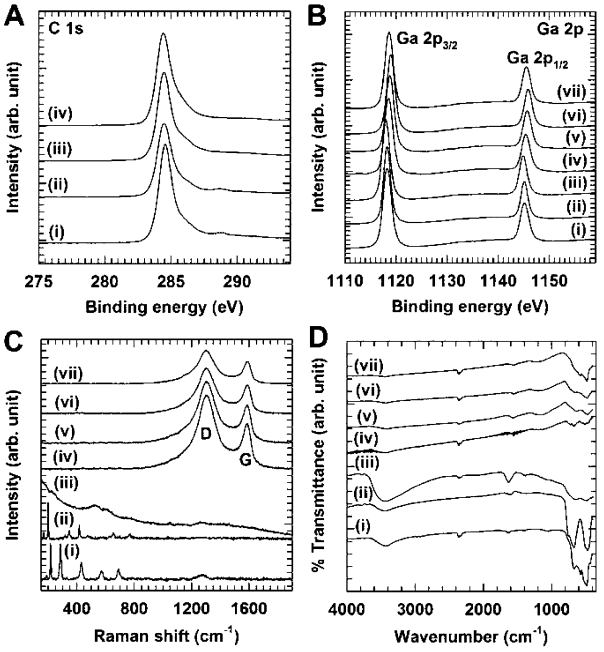

Figure 4. (A) C 1s XPS spectra of Ga_2O_3–rGO nanocomposites with the rGO contents of (i) 25, (ii) 14, (iii) 10, and (iv) 6%. (B) Ga 2p XPS spectra, (C) micro-Raman spectra, and (D) FT-IR spectra of (i) α-Ga_2O_3, (ii) β-Ga_2O_3, and (iii) γ-Ga_2O_3 and the Ga_2O_3–rGO nanocomposites with rGO contents of (iv) 25, (v) 14, (vi) 10, and (vii) 6%.

nanocomposites demonstrate an intense peak at ~284.8 eV in the C 1s XPS spectra, which is assigned as sp^2 carbon species.[28,29] In contrast to the precursor GO showing a prominent peak at ~287.0 eV corresponding to the oxygenated carbon species (Figure S6A), all the present nanocomposites do not show this peak, clearly demonstrating the reduction of the GO precursor upon the composite formation with Ga_2O_3.[28,29] In the Ga 2p XPS spectra, see Figure 4B, the Ga_2O_3–rGO nanocomposites commonly display a slightly higher binding energy than does the unhybridized Ga_2O_3 references, indicating the increase of the hole density of Ga ions. This can be understood as a result of the interaction between oxygen ions of Ga_2O_3 and rGO nanosheets, leading to the weakening of Ga–O bond covalency in the Ga_2O_3. The weakening of Ga–O bond covalency results in the decrease of electron density in Ga ions, which is responsible for the observed displacement of the Ga 2p peaks toward the higher energy side upon hybridization with the rGO nanosheets. All of the nanocomposites demonstrate two distinct and intense Raman features related to rGO species, namely, D band at ~1302 and G band at ~1590 cm^{-1}, underscoring the presence of rGO nanosheets in these materials (Figure 4C).[30] The references of α-Ga_2O_3, β-Ga_2O_3, and γ-Ga_2O_3 exhibit unique phonon lines of metal–oxygen vibrations in the low wavenumber region (<800 cm^{-1}), which are characteristics of their own crystal phases.[31,32] Conversely, there is no Raman feature of metal–oxygen vibration in the Raman spectra of all the Ga_2O_3–rGO nanocomposites, which is attributable to the complete shielding of Ga_2O_3-related Raman features. This clearly demonstrates the intimate coupling of Ga_2O_3 domains with highly conductive rGO species.

As plotted in Figure 4D, the α-Ga_2O_3 and the Ga_2O_3–rGO nanocomposites with the rGO contents of 10 and 6% display a strong IR band centered at 480 cm^{-1} corresponding to the deformation of GaO_6 octahedra with α-Ga_2O_3 phase, whereas an additional IR band corresponding to the stretching and bending modes of GaO_4 tetrahedra at 672 cm^{-1} is observed for the Ga_2O_3–rGO nanocomposites with the rGO contents of 25, 14, and 10%.[33] The observed variation in FT-IR spectra depending on the composition is in good agreement with the phase transition behavior of Ga_2O_3 in the present nanocomposites probed by the XRD analysis. All of the nanocomposites do not show absorption bands related to the oxygenated groups in the GO nanosheets, confirming the conversion of GO to the rGO nanosheets in the composite formation (Figure S6B).[34] Additionally, a small absorption peak corresponding to the C=N stretching mode appears at ~1560 cm^{-1} for all the nanocomposites, strongly suggesting the nitrogen doping in the rGO caused by urea precursor.[35]

3.5. Ga K-Edge XANES and EXAFS Analyses. The local atomic arrangement of Ga_2O_3 in the present Ga_2O_3–rGO nanocomposites is investigated with X-ray absorption near-edge structure (XANES) and EXAFS analyses at Ga K-edge. As plotted in the left panel of Figure 5, all of the present materials

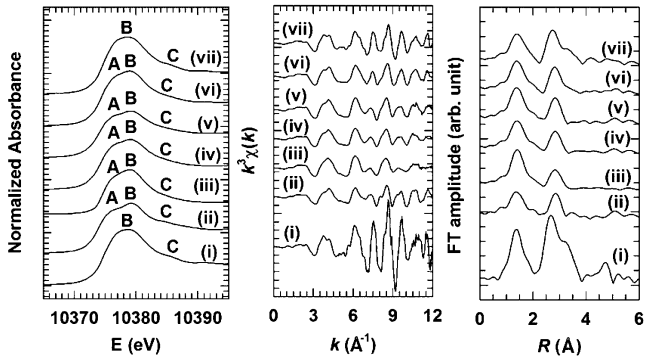

Figure 5. (Left) Ga K-edge XANES spectra, (middle) experimental Ga K-edge EXAFS oscillations, and (right) Fourier-transformed EXAFS spectra of (i) α-Ga_2O_3, (ii) β-Ga_2O_3, and (iii) γ-Ga_2O_3 and the Ga_2O_3–rGO nanocomposites with rGO contents of (iv) 25, (v) 14, (vi) 10, and (vii) 6%.

show main-edge peaks, denoted as A and B, corresponding to the dipole-allowed 1s → 4p transitions, whose spectral features provide sensitive measure for the local structure of Ga ions.[36] The Ga_2O_3–rGO nanocomposite with 6% rGO shows only a peak B corresponding to GaO_6 octahedra, indicating the presence of α-Ga_2O_3 phase in this nanocomposite.[36] Conversely, the nanocomposites with rGO contents of 25, 14, and 10% display both the peaks A and B related to GaO_4 tetrahedra and GaO_6 octahedra, respectively, reflecting the coexistence of α-Ga_2O_3, β-Ga_2O_3, and γ-Ga_2O_3 phases or a comibation thereof.[36,37] A weak postedge peak C is discernible at ~10385 eV for all the present materials, which originates from multiple

DOI: 10.1021/acsami.5b05154
ACS Appl. Mater. Interfaces 2015, 7, 18679–18688

scattering effect by neighboring atoms.[36] While the nanocomposite with 6% rGO shows the similar postedge spectral feature C to the α-Ga_2O_3 reference, the nanocomposites with the rGO contents of 25 and 14% show distinctly different from that of α-Ga_2O_3 but similar to that of β-Ga_2O_3, γ-Ga_2O_3, or both, confirming the formation of β-Ga_2O_3, γ-Ga_2O_3, or both phases with an increase of rGO content.

The overall EXAFS oscillation of the Ga_2O_3–rGO nanocomposite with 6% rGO is quite similar to the reference α-Ga_2O_3 except for the marked depression of amplitude (middle panel, Figure 5). This result suggests the α-Ga_2O_3-type local structure of this material with nanocrystalline nature. In the case of the nanocomposite with 10% rGO, the overall shape of EXAFS signal is in midway of α-Ga_2O_3 and β-Ga_2O_3, reflecting the coexistence of both the phases in this material. The nanocomposite with 14% rGO shows nearly identical EXAFS oscillation to the reference β-Ga_2O_3, indicating the β-Ga_2O_3-type local structure of this material. The EXAFS oscillation of the nanocomposite with 25% rGO is almost the same as that of γ-Ga_2O_3. The Fourier transformed data of Ga K-edge EXAFS spectra are presented in the right panel of Figure 5. All the present Ga_2O_3–rGO nanocomposites demonstrate two distinct FT peaks at ~1.5 and ~2.8–3.5 Å, which correspond to the (Ga–O) and (Ga–Ga) coordination pairs.[36] The observed spectral similarities among the present nanocomposites, α-Ga_2O_3, β-Ga_2O_3, and γ-Ga_2O_3, confirm the gradual phase transformations of hybridized Ga_2O_3 from α-Ga_2O_3 to γ-Ga_2O_3 with decreasing the Ga_2O_3/rGO ratio. The present XANES/EXAFS analysis provides additional strong evidence for the phase transitions of Ga_2O_3 identified by XRD analysis (Figure 1).

3.6. Electrochemical Measurements. The present Ga_2O_3–rGO nanocomposites are applied as anode materials for lithium ion battery to probe their electrode functionality. The overall charge–discharge profile and CV of the Ga_2O_3–rGO nanocomposite appears nearly identical to that of the reference α-Ga_2O_3, strongly suggesting the main contribution of the Ga_2O_3 component to the electrochemical activity of the present nanocomposites (Figure S7). As can be seen from Figure 6A, both the reference α-Ga_2O_3 and γ-Ga_2O_3 materials deliver a huge initial discharge capacity of ~1231 and ~1474 $mAhg^{-1}$, respectively, which are rapidly decreased to <50 and 166 $mAhg^{-1}$ after the 40th cycles. The observed serious capacity fading is ascribed to the irreversible reaction (eq S1) and also to the formation of solid electrolyte interphase (SEI) layer. Conversely, the β-Ga_2O_3 displays large discharge capacity and better capacity retention (~263 $mAhg^{-1}$ for the 40 cycles), underscoring the better electrode performance of β-phase. Also the β-Ga_2O_3 reference shows a higher Coulombic efficiency than the other phases, confirming its better electrochemical stability (Figure 6B). The present findings underscore the importance of the structure control in improving the electrode performance of gallium oxide. All of the present Ga_2O_3–rGO nanocomposites show much weaker capacity fading than does the unhybridized Ga_2O_3 references, indicating the improvement of cyclability upon the composite formation with rGO. Among the present nanocomposites, the best electrode performance occurs for the nanocomposite with 10% rGO showing a large discharge capacity of ~770 $mAhg^{-1}$ after the 40th cycle. This value is comparable to the theoretical reversible capacity of gallium oxide (769 $mAhg^{-1}$), which is sharply contrasted with much smaller capacities of unhybridized Ga_2O_3 materials. An increase of the rGO content from 6 to 10% leads to a significant

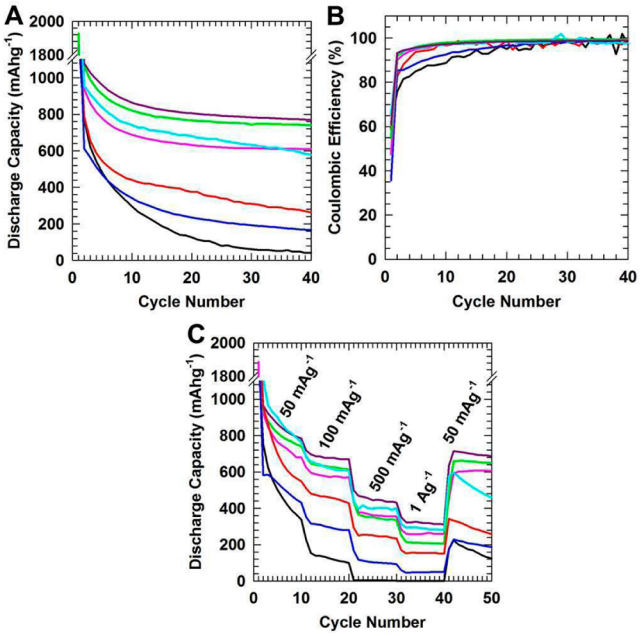

Figure 6. (A) Capacity retention at a current density of 50 mAg^{-1}, (B) Coulombic efficiency, and (C) rate capability of the Ga_2O_3–rGO nanocomposites with the rGO contents of (pink) 25, (green) 14, (dark pink) 10, and (cyan) 6% and the unhybridized references (black) α-Ga_2O_3, (red) β-Ga_2O_3, and (blue) γ-Ga_2O_3.

increase of discharge capacity. As found from the N_2 adsorption–desorption isotherm measurement, the increase of rGO content leads to the increase of the surface area of the nanocomposites. Thus, the remarkable improvement of the electrode performance of Ga_2O_3 upon the hybridization with rGO is attributable to the facilitation of Li ion diffusion caused by the expansion of surface area and the formation of mesopores. However, beyond the 10% rGO, a further increase of the rGO content induces the decrease of discharge capacity even with the gradual increase of surface area. This finding can be interpreted as a result of compromise of the contrasting concentration changes of electrochemically active Ga_2O_3 and highly conductive rGO. In addition, the Ga_2O_3–rGO nanocomposite with 10% rGO possesses the mixed α-Ga_2O_3, β-Ga_2O_3, and γ-Ga_2O_3 phases. Taking into account the fact that the presence of mixed phases is helpful in relieving the volume change of electrode materials during electrochemical cycling compared with single phase, the coexistence of three phases of Ga_2O_3 would make an additional contribution to the improved electrode performance of the nanocomposite with 10% rGO.[38]

As shown in Figure 6B, all the present Ga_2O_3–rGO nanocomposites show much larger Coulombic efficiency of ~100% after the 10th cycle, which is contrasted with the unhybridized Ga_2O_3 references showing lower Coulombic efficiency. This observation provides clear evidence for the improvement of the electrochemical stability of Ga_2O_3 upon the composite formation with the rGO nanosheets. As plotted in Figure 6C, all of the present nanocomposites retain much larger discharge capacity under high current density than do the unhybridized Ga_2O_3 references, underscoring the merit of hybridization in improving the rate characteristic of gallium oxide. Even at the current density of 1 Ag^{1-}, the nanocomposite with 10% rGO retains the large discharge capacity of ~320 $mAhg^{-1}$. This finding clearly demonstrates the usefulness of hybridization with rGO in improving the rate characteristics of

DOI: 10.1021/acsami.5b05154
ACS Appl. Mater. Interfaces 2015, 7, 18679–18688

Ga_2O_3 via the enhancement of electrical conductivity. Among the rGO-free references, β-Ga_2O_3 also delivers a large discharge capacity of ~150 $mAhg^{-1}$ at the high current density of 1 Ag^{1-}, confirming its superior electrode performance.

After the electrochemical cycling, both the powder XRD patterns of the Ga_2O_3–rGO nanocomposite with 10% rGO and reference α-Ga_2O_3 show a complete reduction of Ga_2O_3 into amorphous gallium, which supports the proposed reaction mechanism (eq S1 and Figure S8). The rGO-free α-Ga_2O_3 reference demonstrates a significant agglomeration of particles after electrochemical cycling (Figure S9). However, the nanocomposite with 10% rGO reveals open porous structure with much less agglomeration of electrode particles (Figure S9), which is responsible for improved electrode activity and electrochemical stability compared with the reference α-Ga_2O_3. This finding highlights the importance of rGO in upholding the open porous structure of the electrode with electrochemical cycling in the nanocomposites.

3.7. Possible Intermediate Phases and DFT Calculated Reaction Voltage. The galvanostatic charge–discharge profiles (Figure S7) demonstrate the contribution of two different types of conversion reactions; (a) irreversible conversion reaction of gallium oxide (eq S1) and (b) reversible Li–Ga alloying reaction (eq S2). The reaction energy associated with eq S1 is calculated as −1.26 eV for α-Ga_2O_3, − 1.24 eV for β-Ga_2O_3, and −1.32 eV for γ-Ga_2O_3, leading the theoretical discharge potential of 1.24–1.32 V. From the present CV data (Figure S7), the reduction potential of gallium oxide is measured as 0.6 V, strongly suggesting a substantial amount of overpotential for the Ga_2O_3–rGO nanocomposites. This observation is not surprising because the electrode activity of the present materials is associated with an irreversible conversion reaction. Several phases of GaLi, Ga_2Li_3, and $GaLi_2$ can be considered as possible intermediates during Li–Ga reversible alloying process (Figure S10). All of these phases are available stoichiometric alloys from ICSD having Li atomic content of >50%. The following reaction pathways can be proposed, and the calculated voltage profile is shown in Figure 7:

$$Ga + Li \rightarrow GaLi \quad (1)$$

$$GaLi + \frac{1}{2}Li \rightarrow \frac{1}{2}Ga_2Li_3 \quad (2)$$

$$\frac{1}{2}Ga_2Li_3 + \frac{1}{2}Li \rightarrow GaLi_2 \quad (3)$$

The evolution of charge-transfer behavior upon the hybridization with rGO is examined with EIS. In comparison with the rGO-free α-Ga_2O_3, all of the Ga_2O_3–rGO nanocomposites under investigation demonstrate a significant reduction in the diameter of the semicircle in the high-medium frequency region of the Nyquist plots (Figure S11A). The charge-transfer kinetics of all the materials under investigation are further analyzed by modeling AC impendence spectra based on the Voigt-type equivalent circuit (Figure S11B). The parameters obtained from the fitting analysis are listed in Table S4. The resulting χ^2 function is determined to be very small for all the materials, confirming the good quality of the present fits. The Warburg coefficient σ_w is determined by plotting Z_r vs $\omega^{-1/2}$ in the Warburg region (Figure S11C). All the Ga_2O_3–rGO nanocomposites show much smaller values of R_{ct} and σ_w compared with those of the reference α-Ga_2O_3 (R_{ct} = 438.6 Ω and σ_w = 1602.0 Ω $s^{-1/2}$), underscoring the improvement of the charge-transfer behavior upon the hybridization with rGO. Despite the better charge-transfer kinetics, the nanocomposite with 25% rGO displays inferior electrochemical performance than does the nanocomposite with 10% rGO, which is attributable to the accompanying decrease of the electrochemically active Ga_2O_3 content. The present EIS results confirm that the excellent electrode performance of the Ga_2O_3–rGO nanocomposite with 10% rGO is a result of compromise between the improvement of charge-transfer kinetics caused by the incorporation of the rGO nanosheet and the change of the electrochemically active Ga_2O_3 content with controlled structural phases.

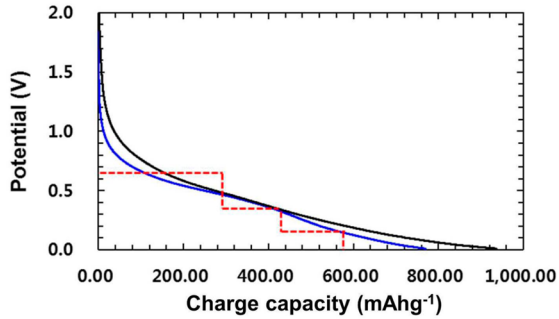

Figure 7. DFT calculated voltage profile (red dashed line) for the proposed conversion reaction pathway eqs 1–3, which is compared with experimental second discharge profile of the nanocomposite with 25% rGO (black line) and that of unhybridized reference α-Ga_2O_3 (blue line).

4. CONCLUSIONS

A phase-controlled synthesis of the Ga_2O_3–rGO nanocomposites can be achieved by the hybridization of Ga_2O_3 with the rGO nanosheets at various Ga_2O_3/rGO ratios. The change of the Ga_2O_3/rGO ratio provides an effective way not only to tailor the crystal structure, crystal morphology, and crystal size of Ga_2O_3 but also to optimize the electrode performance and charge transport of the Ga_2O_3–rGO nanocomposites. This is the first report about the phase control of metal oxide via hybridization with rGO at variable concentrations. The observed promising electrode performance of the present nanocomposites can be ascribed to the improvement of electron transport property through the formation of an open porous structure as well as to the control of crystal structure and morphology through the hybridization with rGO. The present study highlights the usefulness of rGO template for the phase-controlled synthesis of nanostructured metal oxides. Taking into account the promising photocatalytic activity of gallium oxide,[32,39–42] the present nanocomposites are also applicable as photocatalysts for H_2 evolution or the photooxidation of organic compounds. Our current project is the synthesis of other rGO–gallium compound nanocomposites containing gallium chalcogenides, pnicogenides, and hydroxides and their application for electrode materials for lithium secondary batteries and/or photocatalysis.

■ ASSOCIATED CONTENT

Supporting Information

The Supporting Information is available free of charge on the ACS Publications website at DOI: 10.1021/acsami.5b05154.

Powder XRD patterns of the hydroxide counterparts of Ga_2O_3 and all the nanocomposites. The surface

DOI: 10.1021/acsami.5b05154
ACS Appl. Mater. Interfaces 2015, 7, 18679–18688

structures of α- and β-Ga_2O_3 references using DFT calculations. TGA curves of unhybridized α-Ga_2O_3 and all the nanocomposites. XPS and FT-IR spectra of GO and rGO. DFT optimized crystal structures of α-, β-, and γ-Ga_2O_3 references, and lithium intercalated intermediate stages. Powder XRD patterns and FE-SEM micrographs of unhybridized α-Ga_2O_3 and nanocomposite with 10% rGO after electrochemical cycling. Nyquist plots and plots of Z_r vs $\omega^{-1/2}$ in the Warburg region for α-Ga_2O_3 and all the nanocomposites. Lattice parameters of α-, β- and γ-Ga_2O_3 references and their Li intercalated phases with all computational details of DFT calculations. (PDF)

AUTHOR INFORMATION

Corresponding Author

*E-mail: hwangsju@ewha.ac.kr. Tel: +82-2-3277-4370. Fax: +82-2-3277-3419.

Notes

The authors declare no competing financial interest.

ACKNOWLEDGMENTS

This research was supported by the National Research Foundation of Korea (NRF) grant funded by the Korea government (MSIP) (No. NRF-2014R1A2A1A10052809) and Global Frontier R&D Program (2013-073298) on Center for Hybrid Interface Materials (HIM) funded by the Ministry of Science. The experiments at PAL were supported by MOST & POSTECH.

REFERENCES

(1) Geim, A. K. Graphene: Status and Prospects. *Science* **2009**, *324*, 1530−1534.

(2) Wang, Y.; Li, Z.; Wang, J.; Li, J.; Lin, Y. Graphene and Graphene Oxide: Biofunctionalization and Applications in Biotechnology. *Trends Biotechnol.* **2011**, *29*, 205−212.

(3) Kim, I. Y.; Park, S. H.; Kim, H. S.; Park, S. S.; Ruoff, R. S.; Hwang, S.-J. Strongly-Coupled Freestanding Hybrid Films of Graphene and Layered Titanate Nanosheets: An Effective Way to Tailor the Physicochemical and Antibacterial Properties of Graphene Film. *Adv. Funct. Mater.* **2014**, *24*, 2288−2294.

(4) Hlaing, H.; Kim, C.-H.; Carta, F.; Nam, C.-Y.; Barton, R. A.; Petrone, N.; Hone, J.; Kymissis, I. Low-Voltage Organic Electronics Based on a Gate-Tunable Injection Barrier in Vertical Graphene-Organic Semiconductor Heterostructures. *Nano Lett.* **2015**, *15*, 69−74.

(5) Sekar, P.; Anothumakkool, B.; Kurungot, S. 3D Polyaniline Porous Layer Anchored Pillared Graphene Sheets: Enhanced Interface Joined with High Conductivity for Better Charge Storage Applications. *ACS Appl. Mater. Interfaces* **2015**, *7*, 7661−7669.

(6) Zhang, X.; Yang, Y.; Guo, S.; Hu, F.; Liu, L. Mesoporous $Ni_{0.85}Se$ Nanospheres Grown in Situ on Graphene with High Performance in Dye-Sensitized Solar Cells. *ACS Appl. Mater. Interfaces* **2015**, *7*, 8457−8464.

(7) Huang, X.; Qi, X. Y.; Boey, F.; Zhang, H. Graphene-Based Composites. *Chem. Soc. Rev.* **2012**, *41*, 666−686.

(8) Zhang, Z.; Zhang, L.; Li, W.; Yu, A.; Wu, P. Carbon-Coated Mesoporous TiO_2 Nanocrystals Grown on Graphene for Lithium-Ion Batteries. *ACS Appl. Mater. Interfaces* **2015**, *7*, 10395−10400.

(9) Shin, S. I.; Go, A.; Kim, I. Y.; Lee, J. M.; Lee, Y.; Hwang, S.-J. A Beneficial Role of Exfoliated Layered Metal Oxide Nanosheets in Optimizing the Electrocatalytic Activity and Pore Structure of Pt-Reduced Graphene Oxide Nanocomposites. *Energy Environ. Sci.* **2013**, *6*, 608−617.

(10) Lee, J. M.; Kim, I. Y.; Han, S. Y.; Kim, T. W.; Hwang, S.-J. Graphene Nanosheets as a Platform for the 2D Ordering of Metal Oxide Nanoparticles: Mesoporous 2D Aggregate of Anatase TiO_2 Nanoparticles with Improved Electrode Performance. *Chem. - Eur. J.* **2012**, *18*, 13800−13809.

(11) Han, S. Y.; Kim, I. Y.; Jo, K. Y.; Hwang, S.-J. Solvothermal-Assisted Hybridization between Reduced Graphene Oxide and Lithium Metal Oxides: A Facile Route to Graphene-Based Composite Materials. *J. Phys. Chem. C* **2012**, *116*, 7269−7279.

(12) Adpakpang, K.; Oh, S. M.; Jin, X.; Hwang, S.-J. A Direct Hybridization between Isocharged Nanosheets of Layered Metal Oxide and Graphene through a Surface-Modification Assembly Process. *Chem. - Eur. J.* **2014**, *20*, 15459−15466.

(13) Cho, S.; Kim, M.; Jang, J. Screen-Printable and Flexible RuO_2 Nanoparticle-Decorated PEDOT:PSS/Graphene Nanocomposite with Enhanced Electrical and Electrochemical Performances for High-Capacity Supercapacitor. *ACS Appl. Mater. Interfaces* **2015**, *7*, 10213−10227.

(14) Cai, X.; Sakai, N.; Ozawa, T. C.; Funatsu, A.; Ma, R.; Ebina, Y.; Sasaki, T. Efficient Photoinduced Charge Accumulation in Reduced Graphene Oxide Coupled with Titania Nanosheets To Show Highly Enhanced and Persistent Conductance. *ACS Appl. Mater. Interfaces* **2015**, *7*, 11436−11443.

(15) Sung, D.-Y.; Gunjakar, J. L.; Kim, T. W.; Kim, I. Y.; Lee, Y. R.; Hwang, S.-J. Graphene-Assisted Room-Temperature Synthesis of 2D Nanostructured Hybrid Electrode Materials: Dramatic Acceleration of the Formation Rate of 2D Metal Oxide Nanoplates Induced by Reduced Graphene Oxide Nanosheets. *Chem. - Eur. J.* **2013**, *19*, 7109−7117.

(16) Roy, R.; Hill, V. G.; Osborn, E. F. Polymorphism of Ga_2O_3 and the System Ga_2O_3-H_2O. *J. Am. Chem. Soc.* **1952**, *74*, 719−722.

(17) Hummers, W. S.; Offeman, J. R. E. Preparation of Graphitic Oxide. *J. Am. Chem. Soc.* **1958**, *80*, 1339−1340.

(18) Delgado, M. R.; Morterra, C.; Cerrato, G.; Magnacca, G.; Areán, C. O. Surface Characterization of γ-Ga_2O_3: A Microcalorimetric and IR Spectroscopic Study of CO Adsorption. *Langmuir* **2002**, *18*, 10255−10260.

(19) Kresse, G.; Furthmüller, J. Efficiency of Ab-Initio Total Energy Calculations for Metals and Semiconductors using a Plane-Wave Basis Set. *Comput. Mater. Sci.* **1996**, *6*, 15−50.

(20) Perdew, J. P.; Burke, K.; Ernzerhof, M. Generalized Gradient Approximation Made Simple. *Phys. Rev. Lett.* **1996**, *77*, 3865−3868.

(21) Qian, H. S.; Gunawan, P.; Zhang, Y. X.; Lin, G. F.; Zheng, J. W.; Xu, R. Template-Free Synthesis of Highly Uniform α-GaOOH Spindles and Conversion to α-Ga_2O_3 and β-Ga_2O_3. *Cryst. Growth Des.* **2008**, *8*, 1282−1287.

(22) Sreeprasad, T. S.; Maliyekkal, S. M.; Lisha, K. P.; Pradeep, T. Reduced Graphene Oxide-Metal/Metal Oxide Composites: Facile Synthesis and Application in Water Purification. *J. Hazard. Mater.* **2011**, *186*, 921−931.

(23) Zhou, X.; Huang, X.; Qi, X.; Wu, S.; Xue, C.; Boey, F. Y. C.; Yan, Q.; Chen, P.; Zhang, H. In Situ Synthesis of Metal Nanoparticles on Single-Layer Graphene Oxide and Reduced Graphene Oxide Surfaces. *J. Phys. Chem. C* **2009**, *113*, 10842−10846.

(24) He, H.; Orlando, R.; Blanco, M. A.; Pandey, R. First-Principles Study of the Structural, Electronic, and Optical Properties of Ga_2O_3 in Its Monoclinic and Hexagonal Phases. *Phys. Rev. B: Condens. Matter Mater. Phys.* **2006**, *74*, 195123.

(25) Condon, J. B. *Surface Area and Porosity Determinations by Physisorption: Measurements and Theory*, 1st ed.; Elsevier: Amsterdam, 2006; pp 6−14.

(26) Allen, T. *Powder Sampling and Particle Size Determination*, 1st ed.; Elsevier: Amsterdam, 2003; pp 660.

(27) Gunjakar, J. L.; Kim, T. W.; Kim, H. N.; Kim, I. Y.; Hwang, S.-J. Mesoporous Layer-by-Layer Ordered Nanohybrids of Layered Double Hydroxide and Layered Metal Oxide: Highly Active Visible Light Photocatalysts with Improved Chemical Stability. *J. Am. Chem. Soc.* **2011**, *133*, 14998−15007.

(28) Shin, H.-J.; Kim, K. K.; Benayad, A.; Yoon, S.-M.; Park, H. K.; Jung, I.-S.; Jin, M. H.; Jeong, H.-K.; Kim, J. M.; Choi, J.-Y.; et al. Efficient Reduction of Graphite Oxide by Sodium Borohydride and Its

DOI: 10.1021/acsami.5b05154
ACS Appl. Mater. Interfaces 2015, 7, 18679−18688

Effect on Electrical Conductance. *Adv. Funct. Mater.* **2009**, *19*, 1987−1992.
(29) Stankovich, S.; Dikin, D. A.; Piner, R. D.; Kohlhaas, K. A.; Kleinhammes, A.; Jia, Y.; Wu, Y.; Nguyen, S. T.; Ruoff, R. S. Synthesis of Graphene-Based Nanosheets *via* Chemical Reduction of Exfoliated Graphite Oxide. *Carbon* **2007**, *45*, 1558−1565.
(30) Graf, D.; Molitor, F.; Ensslin, K.; Stampfer, C.; Jungen, A.; Hierold, C.; Wirtz, L. Spatially Resolved Raman Spectroscopy of Single- and Few-Layer Graphene. *Nano Lett.* **2007**, *7*, 238−242.
(31) Machon, D.; McMillan, P. F.; Xu, B.; Dong, J. High-Pressure Study of the β-to-α Transition in Ga_2O_3. *Phys. Rev. B: Condens. Matter Mater. Phys.* **2006**, *73*, 094125−094133.
(32) Hou, Y.; Wu, L.; Wang, X.; Ding, Z.; Li, Z.; Fu, X. Photocatalytic Performance of α-, β-, and γ-Ga_2O_3 for the Destruction of Volatile Aromatic Pollutants in Air. *J. Catal.* **2007**, *250*, 12−18.
(33) Rao, R.; Rao, A. M.; Xu, B.; Dong, J.; Sharma, S.; Sunkara, M. K. J. Blueshifted Raman Scattering and Its Correlation with the [110] Growth Direction in Gallium Oxide Nanowires. *J. Appl. Phys.* **2005**, *98*, 094312−094316.
(34) Stankovich, S.; Piner, R. D.; Nguyen, S. T.; Ruoff, R. S. Synthesis and Exfoliation of Isocyanate-Treated Graphene Oxide Nanoplatelets. *Carbon* **2006**, *44*, 3342−3347.
(35) Xue, Y.; Liu, J.; Chen, H.; Wang, R.; Li, D.; Qu, J.; Dai, L. Nitrogen-Doped Graphene Forms as Metal-Free Counter Electrodes in High-Performance Dye-Sensitized Solar Cells. *Angew. Chem., Int. Ed.* **2012**, *51*, 12124−12127.
(36) Nishi, K.; Shimizu, K.-I.; Takamatsu, M.; Yoshida, H.; Satsuma, A.; Tanaka, T.; Yoshida, S.; Hattori, T. Deconvolution Analysis of Ga K-Edge XANES for Quantification of Gallium Coordinations in Oxide Environments. *J. Phys. Chem. B* **1998**, *102*, 10190−10195.
(37) Playford, H. Y.; Hannon, A. C.; Tucker, M. G.; Dawson, D. M.; Ashbrook, S. E.; Kastiban, R. J.; Sloan, J.; Walton, R. I. Characterization of Structural Disorder in γ-Ga_2O_3. *J. Phys. Chem. C* **2014**, *118*, 16188−16198.
(38) Eriksson, T. A.; Lee, Y. J.; Hollingsworth, J.; Reimer, J. A.; Cairns, E. J.; Zhang, X.-f.; Doeff, M. M. Influence of Substitution on the Structure and Electrochemistry of Layered Manganese Oxides. *Chem. Mater.* **2003**, *15*, 4456−4463.
(39) Wang, X.; Shen, S.; Jin, S.; Yang, J.; Li, M.; Wang, X.; Han, H.; Li, C. Effects of Zn^{2+} and Pb^{2+} Dopants on the Activity of Ga_2O_3-Based Photocatalysts for Water Splitting. *Phys. Chem. Chem. Phys.* **2013**, *15*, 19380−19386.
(40) Wang, X.; Xu, Q.; Li, M.; Shen, S.; Wang, X.; Wang, Y.; Feng, Z.; Shi, J.; Han, H.; Li, C. Photocatalytic Overall Water Splitting Promoted by an α-β phase Junction on Ga_2O_3. *Angew. Chem., Int. Ed.* **2012**, *51*, 13089−13092.
(41) Muruganandham, M.; Amutha, R.; Abdel Wahed, M. S. M.; Ahmmad, B.; Kuroda, Y.; Suri, R. P. S.; Wu, J. J.; Sillanpää, M. E. T. Controlled Fabrication of α-GaOOH and α-Ga_2O_3 Self-Assembly and Its Superior Photocatalytic Activity. *J. Phys. Chem. C* **2012**, *116*, 44−53.
(42) Shimura, K.; Yoshida, H. Effect of Doped Zinc Species on the Photocatalytic Activity of Gallium Oxide for Hydrogen Production. *Phys. Chem. Chem. Phys.* **2012**, *14*, 2678−2684.

DOI: 10.1021/acsami.5b05154
ACS Appl. Mater. Interfaces 2015, 7, 18679−18688